XII. MOLECULAR APPLICATIONS (completed)

5. Near/Mid-IR Spectroscopy of Triton/Pluto

The bulk composition of icy, outer solar system bodies provide critical tests of theories concerning the origin of planetary systems. As such, comets, icy satellites, Kuiper belt objects, etc. are of great interest. Two of the more interesting objects in this regard are Triton and Pluto. The composition of Pluto should reflect that of the dust grains from which it was built approximately 30 to 50 AU from the young Sun. Triton's peculiar orbit suggests a similar distance of origin but with a vastly different dynamical history. One has been visited by man's surrogate, Voyager 2, the other has not. What can we learn about these objects by telescopic observations from the Earth?

Methane has been detected on both bodies using the overtone spectra in the far-visible noted in Figure 9.15. As near- and mid-IR detector arrays have improved, our ability to collect vibrational spectra of these objects has improved immensely. Figures 12.35 and 12.36 present the 1-2 μm spectra of Triton and Pluto (see *Science* **261**, pp. 742-748(1993) for more details). These reflectance spectra probe only the upper few mm to cm of the surface. What do they tell us?

Note that CH_4 provides the strongest spectral features, just as it does in the 800-900 nm range. Other features observed in the Triton spectra are due to CO, CO_2, and N_2. On Pluto, similar features are observed in different ratios and profiles *except for CO_2 which is not observed in the IR spectrum of Pluto*. Despite its great intensity, methane is **not** the most abundant molecule on the surfaces of these objects. Recall that as a homonuclear diatomic molecule with no electric or magnetic dipole moment, free N_2 has no vibrational spectrum. By placing it in a matrix, however, the isotropic nature of space is "broken," and a weak vibrational spectrum results. Careful laboratory measurements of the strengths of the various features have been used to demonstrate that the CH_4, CO, and CO_2 abundances are at most a few percent of the N_2 abundance.

Going from these spectra to bulk abundances, which is what the cosmochemical theories are most sensitive to, is very difficult. Indeed, what is suspected to be the most abundant "volatile" on these bodies, water, is not seen in these spectra. This is because water forms hydrogen bonds, which greatly broadens its infrared spectrum. Figures 12.35 and 12.36 were taken with very high spectral resolution and have had a "continuum" subtracted from them. It is very likely that this continuum has contributions both from the solar spectrum as well as very broad absorptions from water ice. Another reason the water ice may not be very visible is due to the surface sampling quality of the reflectance IR spectra. If a large fraction of the surface is covered by the detritus of carbon photochemistry, this hydrocarbon layer may mask the features due to an underlying water substrate. This kind of information is why flybys are so useful when considering disk averaged measurements such as IR and visible reflectance spectra taken with ground-based instruments that necessarily average over what may be a very heterogeneous surface.

In the model I spectrum presented in Figure 12.35, an intimate mix of pure grains are used, with composition and sizes of N_2 99.75%, 8.0 mm; CO 0.10%, 1.0 mm; CO_2 0.10%, 0.8 mm; and CH_4 0.05%, 0.2 mm. Model S uses the same mix of N_2, CH_4, and CO to cover 90% of the surface; with the CO_2 spatially segregated and covering the remaining 10%. Similar data/models are presented in Figure 12.36 for Pluto.
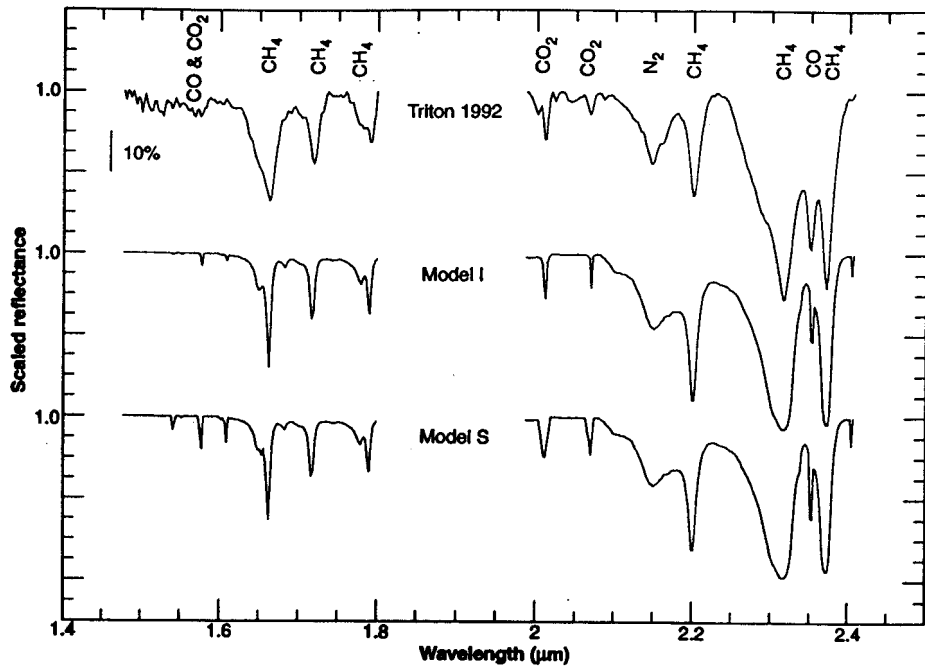
Figure 12.35– The infrared spectrum of Triton from 1.47 to 2.41 μm along with two Hapke scattering models (lower spectra) described in the text. An identification of the various features is presented at right.
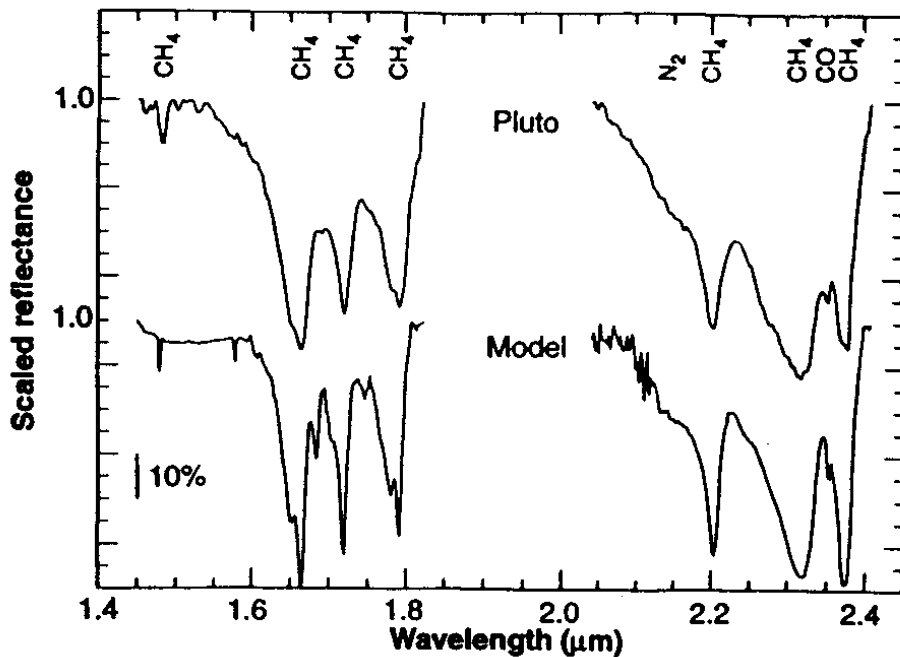

Figure 12.36– A comparison of the continuum-adjusted spectrum of Pluto and a model spectrum based on the indicated mixture of ices over $\lambda = 1.4 - 2.4$ μm. The model below is presented for an intimate mixture of macroscopic grains.

Figure 12.37– The IR spectrum of Triton from $\lambda = 2.07 - 2.18\mu$m (open diamonds). The curves present laboratory-based models with (A) A range of temperature/size fits with 38.9 K/0.43 cm; 37.8 K/0.41 cm; 37.3 K/0.42 cm; and 39.4 K/0.45 cm. (B) Similar models but for a grain size of 0.45 cm at 49.4 and 35.7 K.
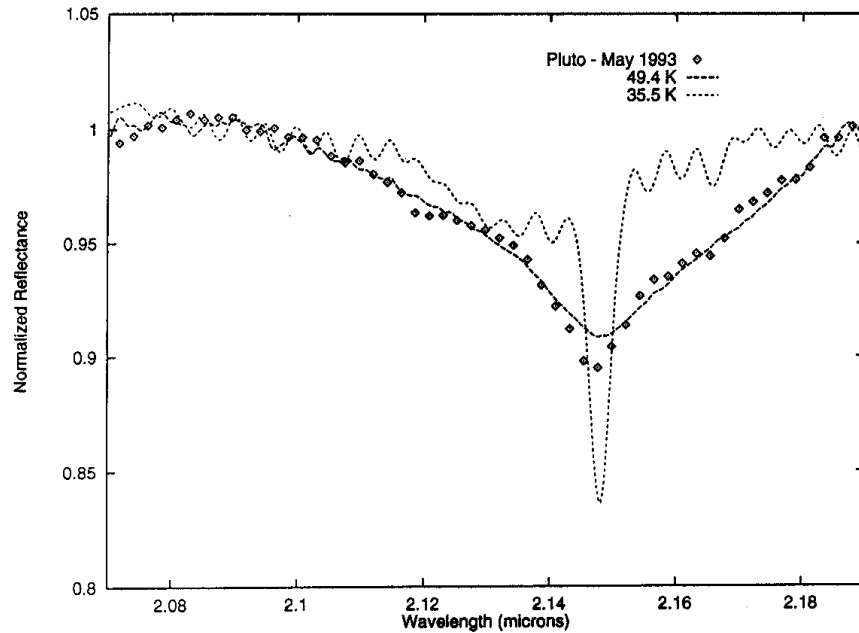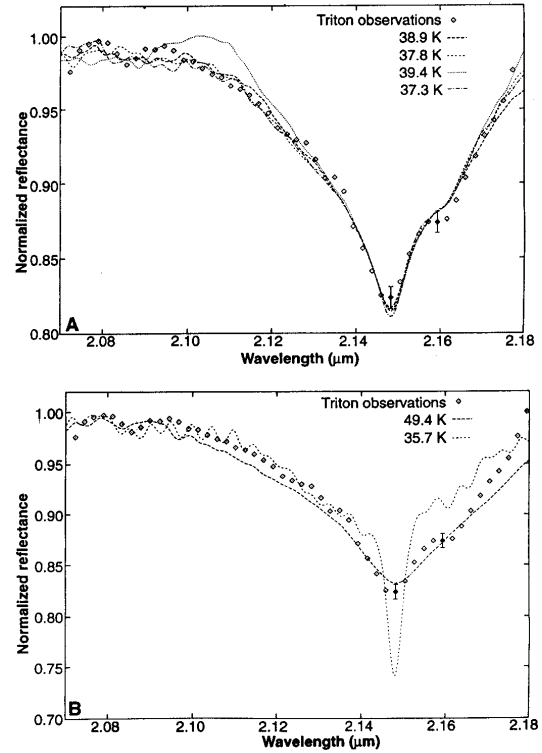

Figure 12.38– Comparison of N_2 band models with the normalized reflectance spectra of Pluto. As for Triton, these models demonstrate that the N_2 is not in the α phase.

Something the N_2 turns out to be quite good at, unexpectedly, is as a surface "thermometer." Tryka et al. have found that the *shape* of the 2.15 μm N_2 band is a sensitive indicator of temperature. Solid N_2 exists in what are called α and β forms. The β phase is a low-density phase of hexagonal structure that is stable only above 35.6 K. Below this temperature and at very low pressures the α phase is more stable. Spectroscopically, the α phase is characterized by an extremely narrow absorption profile below 35.5 K when compared to the β phase. Over a very small temperature range, say 5-10 K, the broad feature characterizing the β phase also has a secondary feature near 2.16 μm. Figures 12.37 and 12.38 present the observed spectra of Triton and Pluto compared with a variety of laboratory spectra and simulations. These measurements yield temperature estimates of 38 and 40 K ($\pm$2 K) for Triton and Pluto. The Triton temperature is in quantitative agreement with that obtained by Voyager 2, and shows that the derived atmospheric pressure of 14 μbar is very close to that expected from vapor-pressure equilibrium for a pure N_2 solid. The Pluto measurements suggest that the bulk of its atmosphere is also contained in molecular nitrogen, not CO (previous mutual occultation data had suggested a mean molecular weight near 28, but could not pin down the actual composition).

6. Maser Observations

Note that in the radiative transfer equations outlined in the section on molecular clouds that describe the line optical depth (eq. 12.42), if the population in the upper state is larger than that in the lower state (or that the level populations are "inverted" with $n_2 > n_1$), the optical depth becomes negative. In this case, any background radiation is amplified and the brightness temperature can attain non-physically high values. Situations such as these lead to *maser* activity, and astrophysical masers are found in the molecular cloud envelopes of mass-losing red giant and supergiant stars, in interstellar molecular clouds, and in the circumnuclear regions of external galaxies. Emission from the most widespread interstellar masers, namely hydroxyl (OH), water (H_2O), and methanol (CH_3OH), is observed toward hundreds of high-mass star-forming regions; H_2O masers are also found toward numerous regions where only low-mass stars are forming. Maser emission from a number of other molecules (chiefly CH, SiO, NH_3, and H_2CO) is observed toward a few high-mass star-forming regions. Because of their very high brightness and compact size, masers can be observed with interferometric techniques are extremely high spatial resolution. In particular, Very Long Baseline Interferometry (VLBI) yields milliarcsecond resolution, allowing mapping of the maser distributions on AU size scales and determination of the three-dimensional velocity fields via proper motion measurements in the star forming clouds near the Sun.

Observed maser intensities are in many cases strongly dependent on the *geometry* of the emitting regions. Thus, it can be difficult infer the physical and chemical conditions within the objects under study beyond certain general constraints. In particular, the known interstellar masers have upper state energy levels between 100-500 K and critical densities between 10^5 and 10^9 $n(H_2)$ cm^{-3}. Clearly, masers are probes of hot, dense regions. In addition, the models of maser emission predict that the high intensities observed require abundances that are significantly larger than those found in isolated dense cores.

Within our own galaxy, the region W3(OH) is the prototypical ultracompact HII region/maser source. A summary of the observational picture is presented in Figure
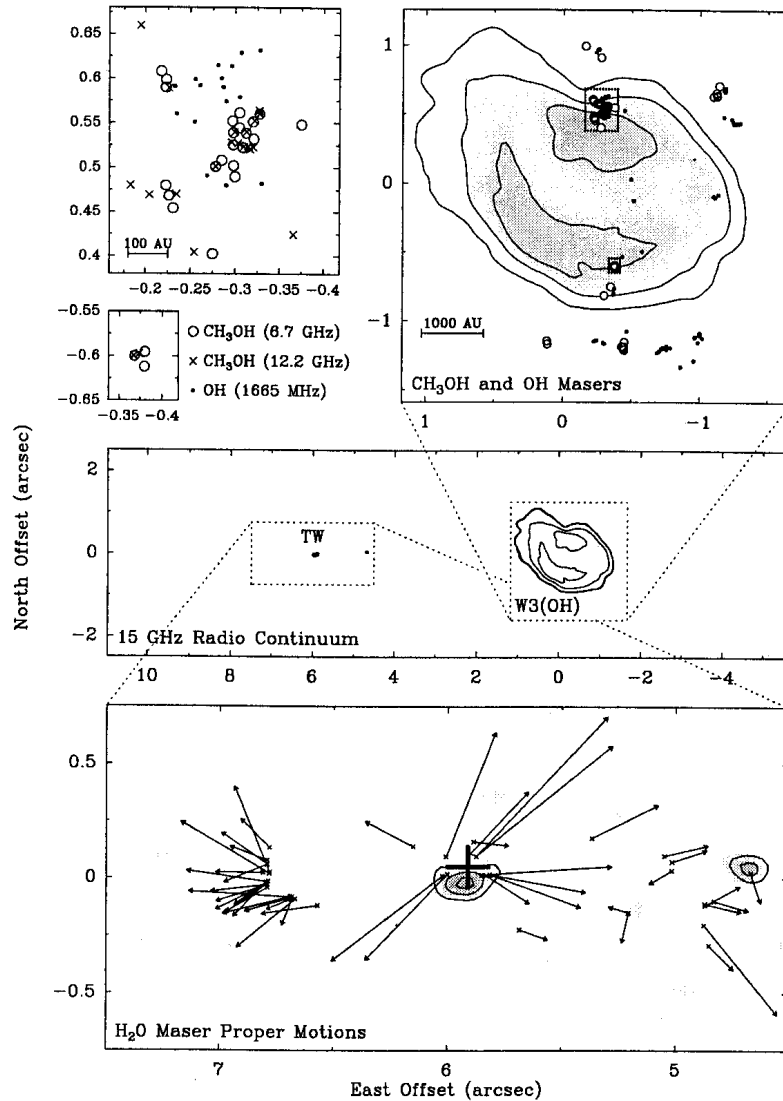
Figure 12.39– Distribution of maser emission from different molecular species toward the ultracompact HII region W3(OH), which dominates the 15 GHz radio continuum map shown in the center panel. In the upper right panel the OH masers are presented as black dots, the CH₃OH masers are shown by the open circles.

12.39. All of the OH and CH₃OH maser spots are found toward the western half of the ultracompact HII region and on scales of 100 AU or less their emission regions overlap. Their radial velocities are also quite similar. In contrast, water masers are not observed toward the ultracompact HII region, but toward a very weak radio continuum source about $6''$ or 0.06 pc east of it that is coincident with a hot, compact dust and molecular line emission core. VLBI proper motion studies have shown that the H_2O masers form a well-defined bipolar outflow whose center of expansion is coincident with the radio continuum source. The continuum emission from this source is non-thermal and most likely represents a jet originating from the young stellar object that is responsible for the outflow.
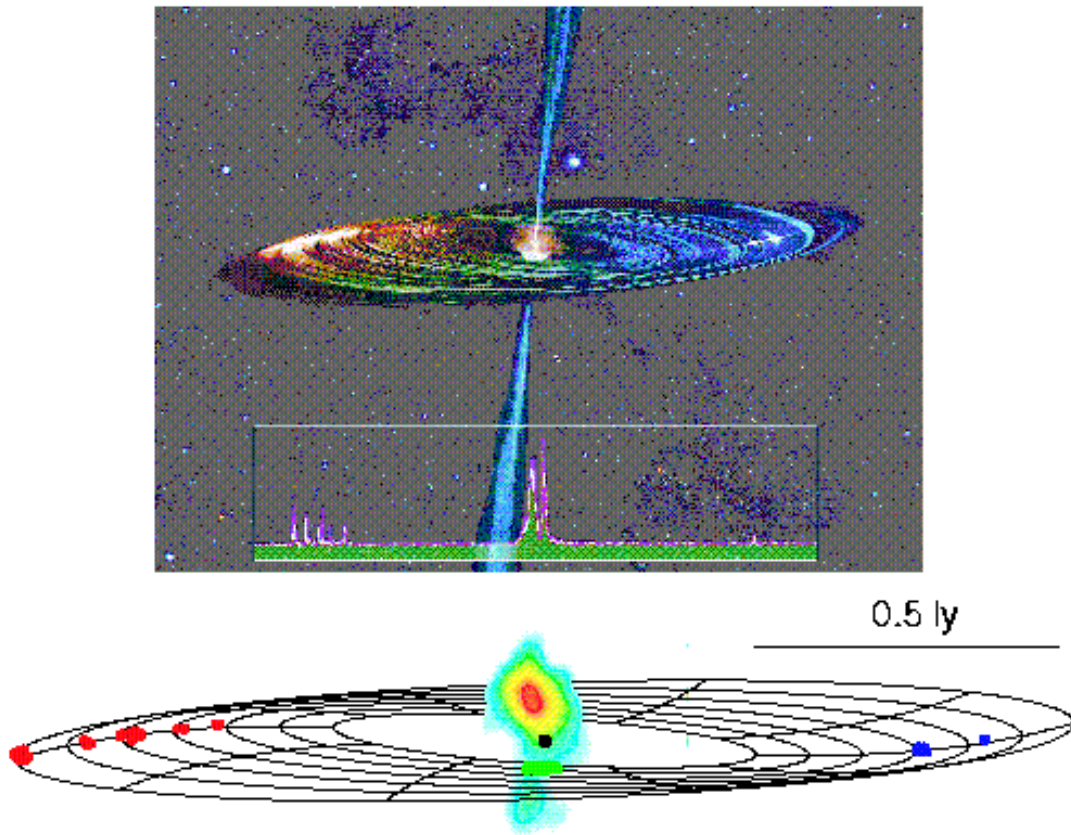
Figure 12.40 The water (H$_2$O) maser and continuum emission from the nearby Seyfert galaxy NGC 4258, also known as Messier 106. Upper panel: A cartoon drawing of the accretion disk surrounding the black hole in NGC 4258 and the synchrotron jet emerging along its spin axis. The spectrum of the H$_2$O maser at 1.3 cm wavelength is shown below. Lower panel. The image of the H$_2$O maser. The wire grid diagram depicts the accretion disk determined from the positions, velocities and accelerations of the maser spots. The continuum emission near the dynamical center of the system appears to be the innermost portion of a jet. Proper motions of the systemic group of masers have been measured at a level of about 32 microarcseconds per year, providing direct evidence of the rotation of the disk as well as a method of determining the distance to the galaxy to an accuracy of 4%. Future kinematical studies of masers around supermassive holes will be greatly enhanced by using the VLBA in conjunction both with the GBT and with orbiting antennas such as VSOP-2, RADIOASTRON and ARISE. Courtesy J. Moran and L. Greenhill (CfA).

Masers have also been discovered toward the centers of AGN and starburst galaxies. As illustrated by Figure 12.40, high precision observations with the Very Long Baseline Array (VLBA) of the positions, velocities, and accelerations of the water vapor masers reveal in detail the dynamical structure of the central molecular disk in the nearby Seyfert galaxy NGC 4258. Although the rotation period of the disk is about 800 years, the high angular (200 μarcsec) and velocity (0.1 km s^{-1}) resolution available with VLBI maser observations allow a tracking of the rotation of the water vapor masers within the disk over a time frame of only a few years (at an accuracy of about 32 μarcsec/year). The molecular material in the center of NGC 4258 traces a very thin disk that is in near-perfect Keplerian rotation over a wide range of radii. The strong emission at low velocities in Figure 12.40 arises from gas along the line-of-site toward the central source; it is the weak emission at high velocities that traces the disk most robustly. The central mass contained within 0.1 parsec exceeds 3×10^7 solar masses, with a mass density exceeding 10^{10} solar masses per cubic parsec. Such a high density is unlikely to be achieved by even the densest stellar cluster, and provides compelling evidence that the central object is a supermassive black hole.

7. Supernova Chemistry

(a) Introduction

When the explosion of supernova 1987 A in the Large Magellanic Cloud was detected on 1987 February 23, it quickly became the most exciting and most studied object in the sky. From our point of view, the most exciting aspect was that it allowed for the first time the observation in detail of atomic and molecular processes which take place within the expanding ejecta of a supernova. The first detection of any molecule in a supernova came with the identification of CO emission in the infrared spectrum of 1987 A, about 100 days after the explosion. The spectrum is reproduced in the Introduction. It consists of the CO vibrational overtone transitions Δv=2, and the (2,0), (3,1), (4,2), ... bands can be clearly distinguished. The identification is confirmed by the fact that the fundamental bands at 4.7 μm are seen as well. In addition, the emission feature at 2.26 μm has been tentatively attributed to the molecular ion CO$^+$, and observations of SiO and CS have recently been claimed.

In order to describe the chemistry in the supernova ejecta, we need a simple physical model. The supernova can be approximated well by a homologously expanding sphere. The radius of the **outer** surface is given by

$$R(t) \;=\; 3.5 \;\times\; 10^{13} t_{\mathrm{day}} \quad \mathrm{cm}, \tag{12.51}$$

and is assumed to expand at the velocity

$$V_{\mathrm{outer}} \;=\; 4100 \;\mathrm{km\ s}^{-1} \,. \tag{12.52}$$

The total number density is a strong function of time, and can be reasonably approximated as

$$n(t) \;=\; 6.5 \;\times\; 10^{16} t_{\mathrm{day}}^{-3} \quad \mathrm{cm}^{-3} \,. \tag{12.53}$$

The velocity of a gas element **interior** to the surface is given by

$$v(r) \;\; = \;\; \frac{r}{R(t)} V_{\text{outer}} \quad \text{km s}^{-1} \; . \tag{12.54}$$

Thus, in the core of the supernova 1987 A, the velocity is roughly $v \sim 500$ km s^{-1}, whereas in the envelope or outer mantle, $v \gtrsim 2000$ km s^{-1}. The velocity of the observed CO emission is consistent with an origin in the core region.

Various models of the structure and composition of the ejecta have been proposed. In the simplest **stratified** model, the ejecta consist of a number of layers, with each shell of material having a constant velocity and composition. An example of such a stratified or "unmixed" model is shown in Figure 12.16. The inner core consists mostly of ^{56}Ni, followed by Si, O and He layers. The CO emission would then occur mostly from the oxygen layer of the core.

After the supernova exploded, the ^{56}Ni decayed into ^{56}Co and ^{56}Fe:

$$^{56}\text{Ni} \quad \rightarrow \quad ^{56}\text{Co (77 days)} \quad \rightarrow \quad ^{56}\text{Fe} \;\; , \tag{12.55}$$
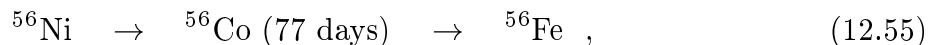
where the decay of ^{56}Co was predicted to be accompanied by γ-ray lines at 847 and 1238 keV. The interaction of the γ-rays with the gas subsequently leads to X-rays and optical radiation. The γ-rays and X-rays were indeed detected from SN 1987 A, but about six months earlier than the fully stratified model shown in Figure 12.41 predicted. The early emergence of the γ-rays can only be accounted for in a *"mixed"* model, in which the light and heavy elements are mixed. An example of such a mixed model, which fits the observations of SN 1987 A, is shown in Figure 12.42. According to this model, the density at 100 days after the explosion was of order 10^{11} cm^{-3}, and the composition of the core is summarized in Table 12.8.

<div align="center">

Table 12.8– Composition of the Core of SN 1987 A "Mixed" Models

</div>

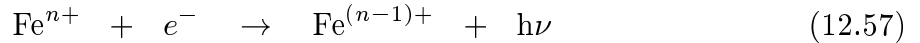| Element	M(M$_\odot$)
He	2.5
O	1.1
H	0.42
Si	0.21
C	0.16
S	0.13
Co	0.059
Fe	0.059

(b) Chemistry in the Core of SN 1987 A

The velocity of the observed CO emission suggests that it originates mostly in the inner core of the ejecta. The observed CO vibrational excitation can be described by a temperature of about 3000 K at day 192, decreasing to about 1200 K by day 349. It is assumed that the gas temperature is the same as the temperature inferred from these CO observations.

What is the chemistry that occurs in this region? First, it is important to note that the infrared spectrum (see Introduction) shows no highly ionized material, but only atomic lines from neutral and singly ionized species. At first sight, this may seem somewhat unexpected, since the X-rays produced in the radioactive decay can be absorbed by the heavy elements. In particular, we have seen in § IV.A that they can lead to efficient multiple ionization through **Auger** process such as
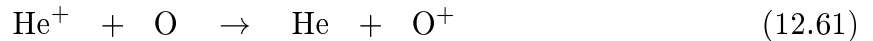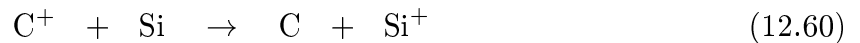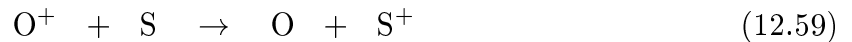
$$\text{Fe} \; + \; \text{X} - \text{ray} \quad \rightarrow \quad \text{Fe}^{n+} \; + \; ne^- \; . \tag{12.56}$$
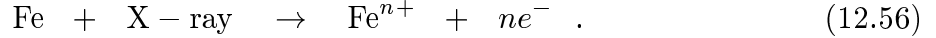
The ionization can be reduced by recombination,

$$\text{Fe}^{n+} \; + \; e^- \quad \rightarrow \quad \text{Fe}^{(n-1)+} \; + \; \text{h}\nu \tag{12.57}$$

and, more importantly, by charge transfer. The latter process quickly drives the ionization to the element with the lowest ionization potential. For the elements produced in the core, the order of the ionization potentials is

$$\text{He} > \text{O} > \text{C} > \text{S} > \text{Si} > \text{Fe} > \text{Co} > \text{Ni} \; . \tag{12.58}$$
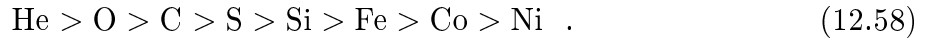
Thus, e.g. O^+ will transfer its charge to sulfur, which in turn will transfer its charge to Fe, Co, and Ni. As a result, elements like O and C are mostly neutral in the core, whereas Ni is mostly ionized. However, as noted before, the rate coefficients for charge-transfer reactions of singly-charged and neutral species are uncertain. The process is only fast if favorable curve crossings, such as illustrated in Figure 11.20, occur. Unfortunately, for many of the systems of interest, such as

$$\text{O}^+ \; + \; \text{S} \quad \rightarrow \quad \text{O} \; + \; \text{S}^+ \tag{12.59}$$

$$\text{C}^+ \; + \; \text{Si} \quad \rightarrow \quad \text{C} \; + \; \text{Si}^+ \tag{12.60}$$

$$\text{He}^+ \; + \; \text{O} \quad \rightarrow \quad \text{He} \; + \; \text{O}^+ \tag{12.61}$$

the potential curves are not well known. It is assumed that most of these reactions are fast, with $k \sim 10^{-9}$ cm^{3}s^{-1}, but that reactions with He$^+$ are slow. For the case of reaction (12.33), the rate coefficient has been estimated to be only of order 10^{-13} cm^{3}s^{-1}. Thus, whereas O, C, S, ... are mostly neutral, He$^+$ ions are still present in the core.

It is instructive to compare the chemistry in supernova ejecta with that occurring in interstellar clouds. In interstellar clouds, the gas is hydrogen rich and H$_2$ is formed on the surfaces of grains. The gas is cold, T$\sim$10-20 K, the density is about $n \sim 10^4$ cm^{-3}, and the fractional ionization is very low, $n_e/n_{\text{H}} \lesssim 10^{-7}$. In the supernova, the gas is very hydrogen poor, and initially there are no grains. The gas is hot, T$\sim$3000 K, and both the densities and the fractional ionization are high ($n \sim 10^{11}$ cm^{-3} and $n_e/n \sim 10^{-1}$), because of the presence of the γ-rays.

Although the density in the supernova ejecta is high, it is not large enough for 3-body reactions to occur with any significance. Thus, the molecule formation must be initiated
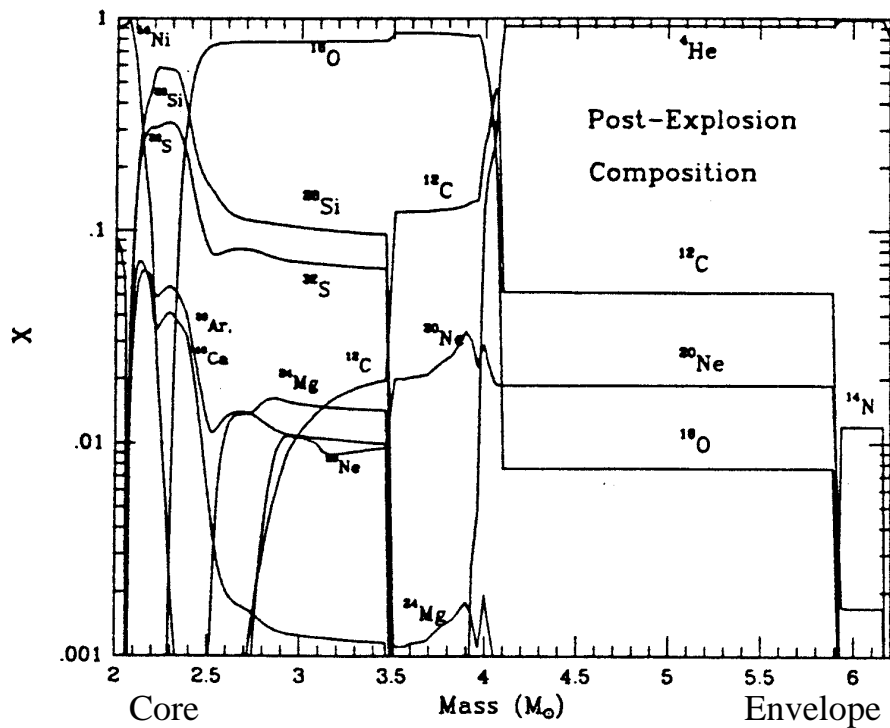
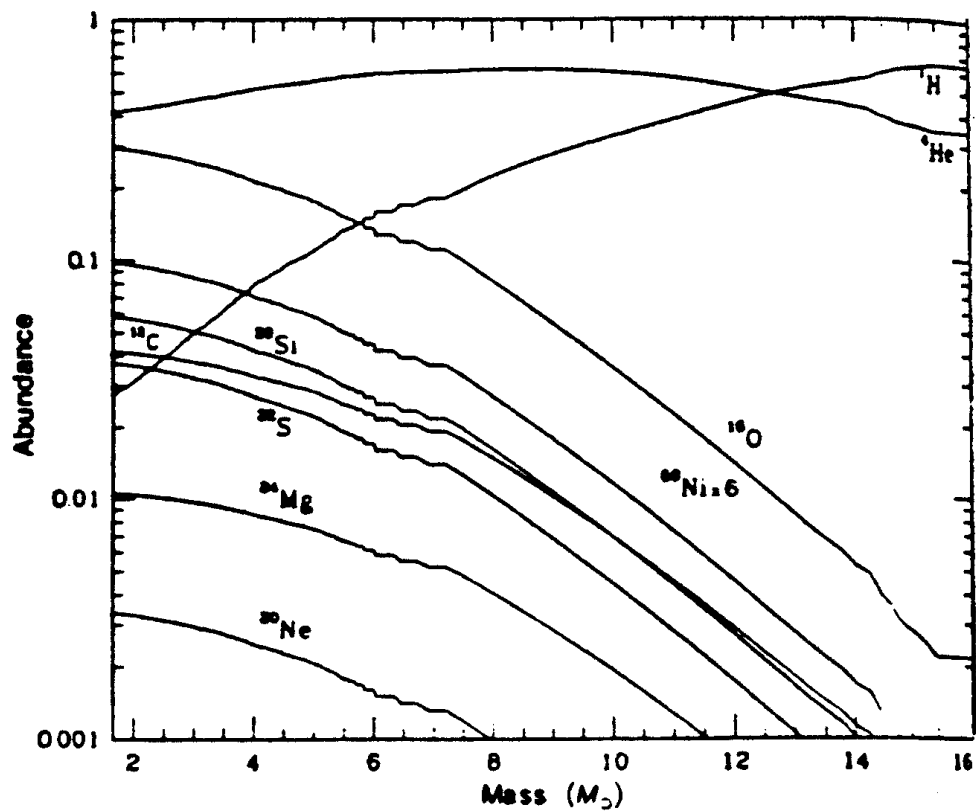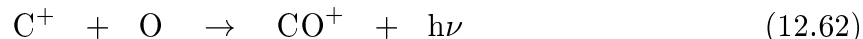**Figure 12.41–** Stratified or unmixed supernova model.


Figure 12.42– Unstratified or mixed supernova model.

by radiative association or radiative attachment. The principle initiating reaction was thought to be the radiative association reaction

$$C^+ \; + \; O \quad \to \quad CO^+ \; + \; h\nu \tag{12.62}$$

which, if followed by the charge-transfer reaction

$$CO^+ \; + \; O \quad \to \quad CO \; + \; O^+ \tag{12.63}$$

can lead to the formation of both CO and CO^+. However, detailed calculations of the rate coefficient for reaction (12.34) indicate that it is very slow, only on the order of 2×10^{-18} cm^3s^{-1} at the relevant temperatures. The formation of CO by direct radiative association

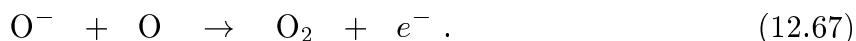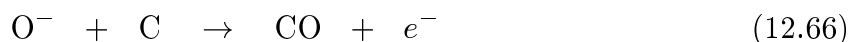$$C \; + \; O \quad \to \quad CO \; + \; h\nu \tag{12.64}$$
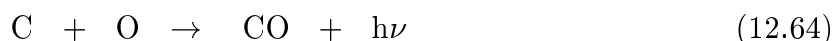
is also not very efficient, $k \sim 3 \times 10^{-17}$ cm^3s^{-1}, and its rate coefficient drops rapidly at low temperatures.
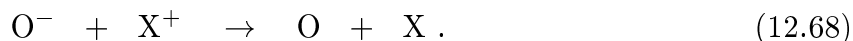
An alternative formation route to CO starts with the radiative attachment reaction

$$O \; + \; e^- \quad \to \quad O^- \; + \; h\nu \tag{12.65}$$
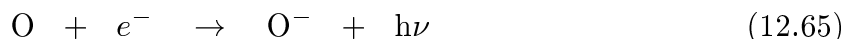
followed by the rapid associative reactions

$$O^- \; + \; C \quad \to \quad CO \; + \; e^- \tag{12.66}$$

$$O^- \; + \; O \quad \to \quad O_2 \; + \; e^- \;. \tag{12.67}$$

However, the abundances of O^- is limited by rapid photodetachment and by mutual neutralization

$$O^- \; + \; X^+ \quad \to \quad O \; + \; X \;. \tag{12.68}$$

If some hydrogen is mixed into the core, as is assumed in the model of Figure 12.17, CO can also be formed by a sequence of reactions which starts with the radiative association reaction

$$He^+ \; + \; H \quad \to \quad HeH^+ \; + \; h\nu. \tag{12.69}$$
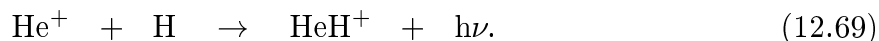
This reaction is relatively rapid, $k \sim 10^{-15}$ cm^3s^{-1}, and HeH^+ is not lost by rapid dissociative recombination (see § XI.2), so that reasonable amounts of HeH^+ can be formed. HeH^+ subsequently leads through a series of rapid reactions to CO:

$$HeH^+ \; + \; H \quad \to \quad H_2^+ \; + \; He \tag{12.70}$$

$$H_2^+ \; + \; H \quad \to \quad H_2 \; + \; H^+ \tag{12.71}$$

$$H_2 \; + \; O \quad \to \quad OH \; + \; H \tag{12.72}$$

$$C \; + \; OH \quad \to \quad CO \; + \; H \tag{12.73}$$

$$C^+ \; + \; OH \quad \to \quad CO^+ \; + \; H \tag{12.74}$$
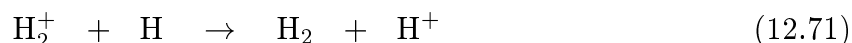
The CO that is formed by these different routes is rapidly destroyed by its reaction with He^+

$$He^+ \ + \ CO \ \rightarrow \ He \ + \ C^+ \ + \ O \ . \qquad (12.75)$$
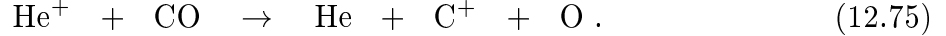
Alternative destruction routes of CO include photodissociation and the reverse of reaction (12.63).

What are the results of these models? The CO abundances can be computed at each day separately, with the densities given by equation (12.25) and the temperature by the observed CO vibrational temperature. At t <500 days the density is so high that the chemical time scales are short compared with the expansion time, and a steady-state description suffices. At t <70 days, no molecules survive because the temperature is still so high that collision-induced dissociation destroys all the CO molecules.

The exact predictions of the models depend sensitively on the degree of element mixing and on the rate of charge-transfer for reactions of He^+ with other species (such as reaction (12.61)). At early times, t ~70-100 days, radiative association of C + O is the dominant source of CO, but at later times as the temperatures and densities fall the sequences initiated by the formation of H_2 and OH become more effective – if the He^+ indeed reacts slowly with other species. If He^+ undergoes rapid charge transfer, the C + O radiative association reaction is dominant throughout. The negative ion chemistry is not a major source of molecules in this model. At all times, the destruction of CO is dominated by the reaction with He^+

Table 12.9– CO Temperature and Mass in SN 1987 A Fully Mixed Model

Epoch (days)	Observed[1]		Calculated		
	Temp. (K)	Mass $(M_\odot)$	Mass $(M_\odot)$[2]	Mass $(M_\odot)$[3]	Mass $(M_\odot)$[4]
192	3000	1.7×10^{-5}	6.3×10^{-7}	1.9×10^{-6}	6.8×10^{-5}
255	1800	4.7×10^{-5}	4.8×10^{-7}	1.7×10^{-6}	4.6×10^{-5}
284	1600	1.2×10^{-4}	4.7×10^{-7}	1.8×10^{-6}	4.5×10^{-5}
349	1200	8.0×10^{-5}	4.1×10^{-7}	1.7×10^{-6}	2.8×10^{-5}

[1] from Spyromilio et al. (1988)

[2] Standard model.

[3] with $k_{He^+ + Si} = 3.3 \times 10^{-9} cm^3 s^{-1}$

[4] with $k_{He^+ + Si} = 3.3 \times 10^{-9} cm^3 s^{-1}$ and the ionization rate reduced

by a factor of two.

Table 12.9 compares the results of this so-called standard mixed model with the observations of CO. It is seen that the model CO abundances are smaller than the observed abundances by 1-2 orders of magnitude. The principal reason for this is probably the high

He$^+$ abundance in the model, which destroys CO. If some of the reactions of He$^+$ with other species were rapid, e.g. if

$$He^+ \quad + \quad Si \quad \rightarrow \quad He \quad + \quad Si^+ \tag{12.76}$$
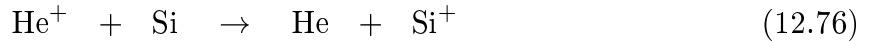
proceeded with k $\sim 10^{-9}$ cm^{3}s^{-1}, the He$^+$ abundance would be reduced and the CO abundance increased. Alternatively, a reduction in the ionization rate of He could bring the models into agreement with observations, as Table 12.8 shows.

Although the CO abundances may be reproduced by postulating fast charge transfer of He$^+$ with heavier atoms, a more likely model, which is also successful in reproducing the observed CO mass, retains low rate coefficients for charge transfer of He$^+$, but lessens the element mixing. In the unmixed, stratified model illustrated in Figure 12.41, there are regions of high oxygen and carbon abundance with little helium. Such a model leads to a CO abundance of 10^{-2} M$_\odot$, considerably in **excess** of the observed mass! The observed abundances can be reproduced by an intermediate model with small, isolated regions of unmixed material containing only about one percent of the gas.

Note that the chemical models also lead to significant abundances of O$_2$, H$_2$, CS, HeH$^+$, SiO, and OH, but they do not seem to produce enough CO$^+$, if the feature at 2.26 μm is indeed due to this ion. However, the observed abundance of CO$^+$ may well have been overestimated; the dipole derivatives must be calculated from theory.

(c) Chemistry in the Outer Envelope of SN 1987 A

The outer envelope of supernovae is mostly hydrogen, as Figure 12.42 shows, with other elements present in small abundances. The chemistry in this region is similar to that found, e.g., in the early Universe. The densities are still high enough, n $\sim 10^8$ - 10^{11} cm^{-3}, that two-body reactions are rapid compared with expansion.

H$_2$ can be formed in the outer envelope by both the H$^+$ sequence (reactions (12.8)-(12.9)) and the H$^-$ sequence (reactions (12.13)-(12.15)) discussed in § XII.1. Subsequent reactions with C and O then lead to CH and OH, which, in turn, can result in CO through reactions (12.44)-(12.45), and similar reactions for CH. If the ionization fraction in the envelope is low, most of the atomic carbon and a large fraction of the atomic oxygen are rapidly converted into CO. Most of the hydrogen remains in atomic form, however. Figure 12.43 shows the results of such a calculation.

On the other hand, if the gas is ionized by the γ-rays and X-rays as in the core, the CO can be rapidly destroyed by reactions with He$^+$, and its abundance is reduction to only a fraction, about 10^{-3} of the carbon. Nevertheless, it is clear that significant amounts of CO can also be produced in the rapidly expanding envelope. However, because of the large velocity of the envelope, $v \gtrsim 2000$ km s^{-1}, the emission at each wavelength is reduced, so that the intensity is spread out over a broader band profile. Thus, it may still contribute only a small amount to the observed flux at 2.3 μ, which is mostly due to he CO in the core.

These models show that molecule formation can take place in extreme environments, and the chemistry in supernova ejecta is similar to that found in the early Universe or in high-velocity protostellar winds. Indeed, the chemistry of the supernova envelope resembles that of the protostellar wind modelled by Glassgold *et al.* (1989, *Ap. J.* **336**, L29).
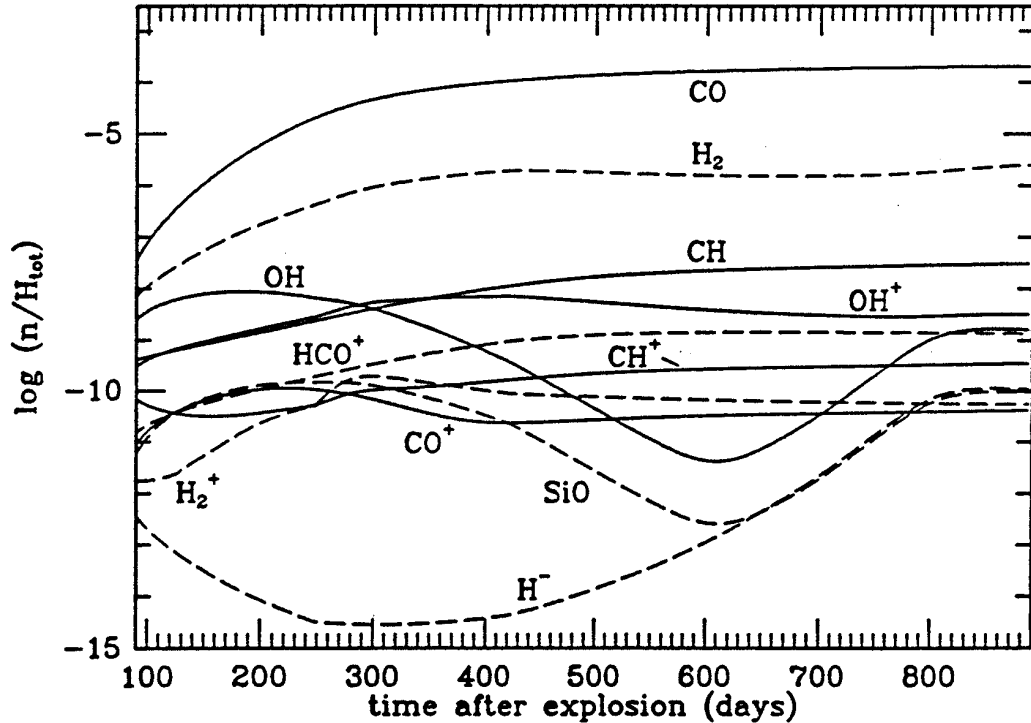
Figure 12.43– Molecular abundances versus time (in days) after detonation of SN 1987 A. Number abundances are w.r.t. hydrogen in all forms. Elemental abundances are 0.25 times solar with O enhanced. There is no hydrogen depletion, and the cooling is adiabatic. The initial temperature and density of $T_o = 5000$ K and $n_o = 10^{11}$ cm^{-3} have dropped to $T_f = 225$ K and $n_f = 8.3 \times 10^7$ cm^{-3} at 887 days.

A qualitatively similar result is that hydrogen remains primarily atomic while a large fraction of the heavy elements are converted into molecules. The expansion velocity of the supernova is more than an order of magnitude faster, however. It can now be argued that significant molecular abundances are likely to form in a variety of other extreme environments. The key requirement is that the rate of molecular synthesis be faster than the rate of expansion (or collapse). In both the supernova envelope and protostellar winds, *in situ* formation of molecules may be important to our understanding of the emission from these regions. Molecular emission need not arise from pre-existing material swept up in the expansion.

References

Lepp, Dalgarno, and McCray 1990, *Ap. J.* **358**, 262.

McCray, R. 1990, in *Molecular Astrophysics*.

McCray, R. & Li, H.W. 1989, in *Structure and Evolution of Galaxies*, ed. F. Li Zhi (Singapore World Science Publ. Co.)

8. Whole Disk Spectroscopy of Planetary Atmospheres/Exoplanetary Science

Over the 1995 calendar year, scientists uncovered the existence of Jovian-class planets around three main sequence stars: 51 Pegasi, 70 Virginis, and 47 Ursa Majoris. To date, more than eighty have been discovered, and the rate of discovery continues unabated. As optical/IR interferometric techniques are optimized and placed into near-earth orbit it will become possible to detect terrestrial-class planets out to distances as great as 20-30 parsecs. Clearly, over the course of our lifetime planetary science will become *comparative* in nature. At the great distances which characterize even the nearest extra-solar planetary systems, it will not be possible to generate images of the new planets (images of the orbits, yes, but not the planets themselves). How then are we to characterize them?

The orbital motions, when corrected for effects such as inclination, will tell us about the mass ranges of the planets. This will clearly be a long term effort, requiring a great deal of time and dedication. Spectroscopy offers another means of characterizing planets, one which has had a long and rich history in the exploration of our own solar system. Figure 12.44 illustrates the magnitude of the challenge to be surmounted, namely the rejection of the overwhelmingly larger number of photons from the central star. Looking forward to such spectra, however, we review below some of the "highlights" of the whole disk spectra of planetary atmospheres from both Jovian and terrestrial planets.

a) The Jovian Planets

Overviews of the infrared spectra of the planets were presented in Figures 9.22 and 9.23. These are so-called whole disk spectra, in which emission from the entire planet is collected and displayed; and it is these sort of spectra that would be collected for any extra-solar planetary system. In Figure 9.23 the spectral intensities are plotted as brightness temperature, since for the Jovian planets there is no solid surface, and the emission observed arises from levels where the species of interest becomes optically thick.

At long wavelengths, the dominant features between 200-800 cm^{-1} arise from collision-induced rotational features of molecular hydrogen. They arise from both H_2-H_2 and H_2-He collisions, and their shape can be used to infer the H_2/He ratio in the upper atmosphere. Further into the IR the prominent Q-branch of acetylene near 723 cm^{-1} is evidence of an increasing C/H ratio as one moves out in the solar system (look carefully at the Jupiter/Saturn spectra).

In the mid- and near-IR (1000-10,000 cm^{-1}), transitions of ammonia and methane dominate the spectra of Jovian planets. As we saw in Figure 9.22, these spectra are intrinsically unresolvable at the pressures and temperatures which characterize Jupiter and Saturn. As the planets get larger, or if we were to view Jupiter much earlier in its history, the atmosphere would be substantially hotter and the spectra would become even more congested. Somewhere between Jupiter and the Sun lies the world of brown dwarfs, not quite planets and not quite stars. Recently, Caltech scientists have recorded the first spectra of brown dwarfs, both as companions to stars and as free floating objects. The very first unambiguous brown dwarf detected, called GL229B, has a spectrum reminiscent of the Jovian planets, as illustrated by the near-IR data presented in Figure 12.45. We note that the higher temperatures will make the spectrum very complex at these wavelengths, and much laboratory work remains to be done before such spectra are completely understood.
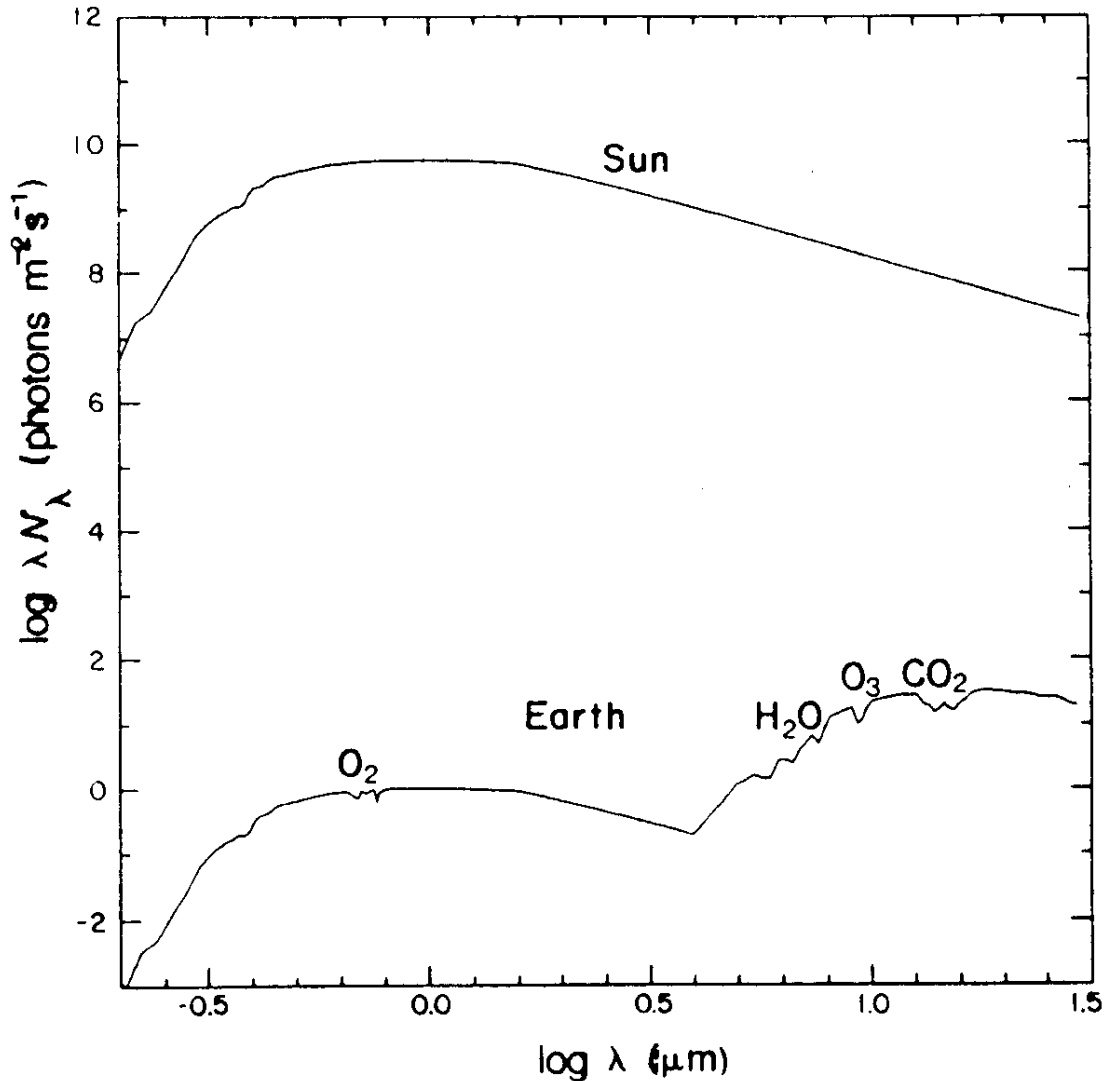
Figure 12.44– Fluxes of the Sun and Earth as seen from 4 pc. Detection of spectral features in the shot noise limit depends on the photon flux in a given bandwidth, hence the quantity is plotted as $\log(\lambda N_\lambda)$. The Earth's optical flux assumes a constant albedo of 0.4 and isotropic emission. The IR features are normalized to be consistent with re-radiation of 60% of the absorbed sunlight.

A spectacular example of how high temperatures and chemical processes can effect the spectra of planetary atmospheres was provided by the recent impact of comet Shoemaker-Levy 9 (SL9) with Jupiter. The next few spectra review some of the wide range of features observed either just after the collision or for a brief period of time after the collision sequence. Good overviews of the observations and results may be found in the 3March1995 issue of *Science* and the 15June1995 issue of *Geophysical Research Letters*.

In the ultraviolet, lines of metallic species are seen immediately after the impact, and at longer time sulfur-containing molecules come to the fore. There is too much sulfur to be from the impactor, and so must be derived from the sulfate-ammonium cloud deck on Jupiter near 1-2 bars (ammonia is also seen). Interesting, oxygen-containing species were
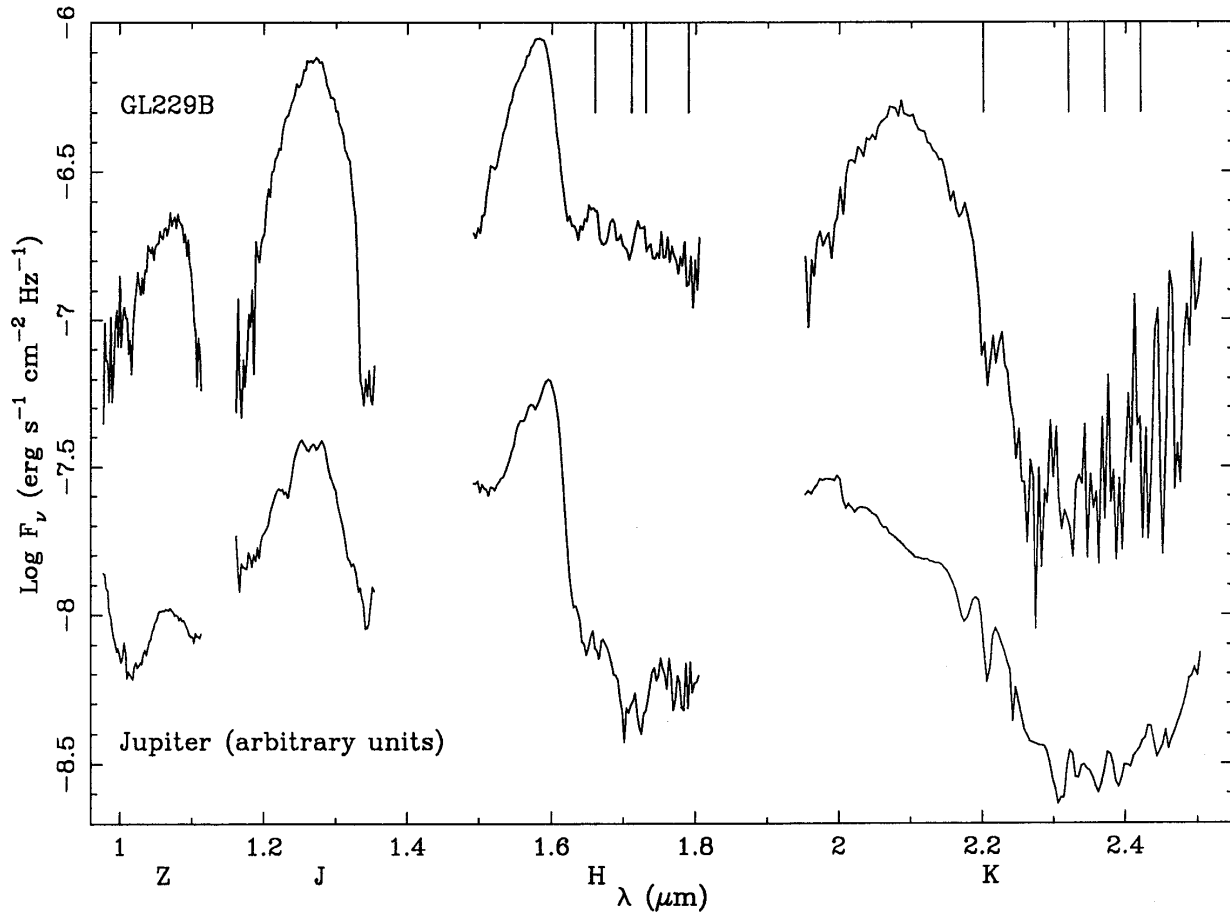
Figure 12.45– Near-IR spectra of the brown dwarf GL 229B and of Jupiter. The spectra of Jupiter are positioned vertically simply for easy of comparison. The spectral resolution is 150, and the vertical bars at the top of the plot indicate the locations of CH_4 absorption features at 1.66, 1.71, 1.79, 2.20, 2.32, 2.37, and 2.4 μm.

not seen, a harbinger of the fascinating Galileo probe descent data which reveal a dry atmosphere to many bars.

At near- and mid-IR wavelengths, broadband observations were used to constrain the temperature histories of the fireballs, while observations at higher spectral resolution - not surprisingly - revealed a wealth of emission from ammonia and methane. The methane bands are extraordinarily rich, characterized by very high rotational and vibrational temperatures in the aftermath of the impacts. As is the case with brown dwarfs, the laboratory data and spectral simulations are not yet up to the task of verifying all of the features quantitatively.
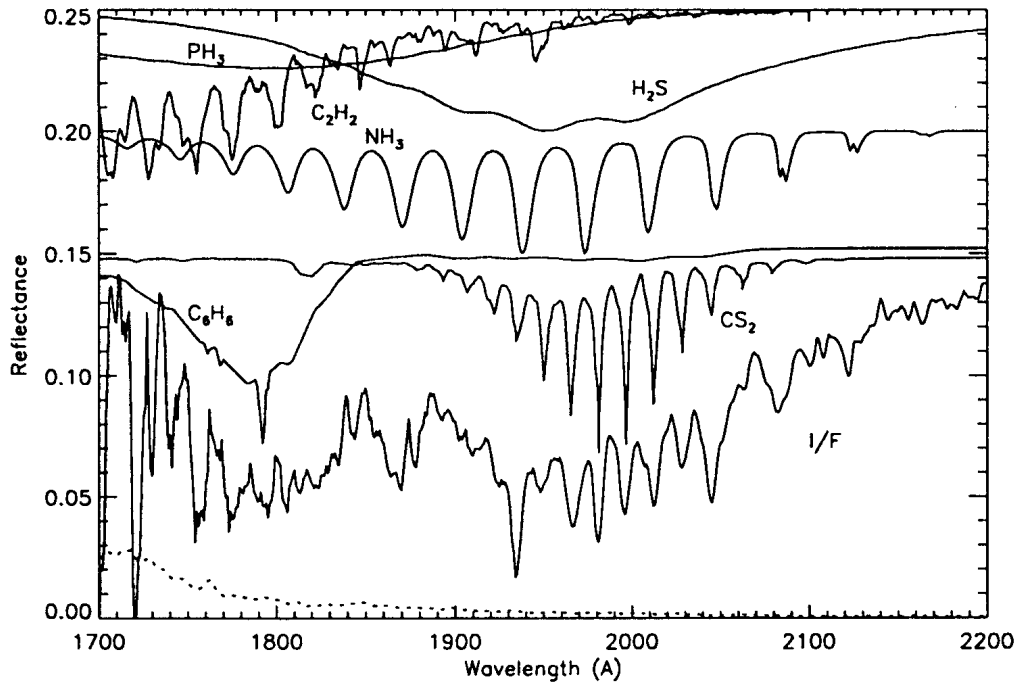
Figure 12.46– Reflectance vacuum UV spectra of the SL9 impact zones between 1700 - 2200 Å (1/F, where πF is the solar flux at Jupiter). The cross sections of various potential compounds in the atmosphere are plotted as well, since the transmission of light through the atmosphere is proportional to this quantity. The spectral resolution is 3.3 Å.
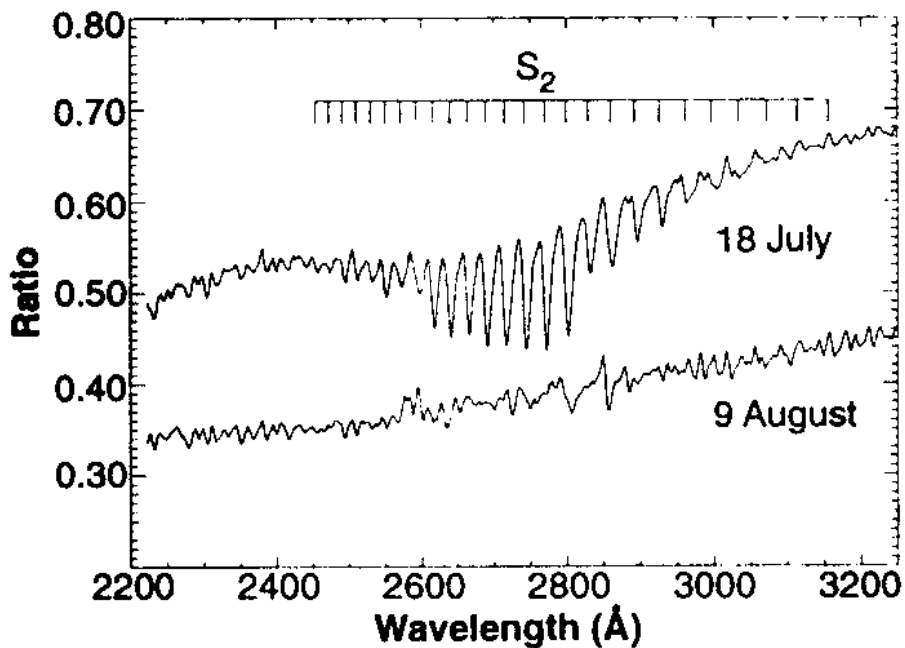

Figure 12.47– Near UV spectra of pre- and post-SL9 impact zones, dominated by the B $^3\Sigma_u^- \leftarrow$ X $^3\Sigma_g^-$ transition of S_2. The spectral resolution is 9.3 Å.

Table 12.10 - Derived abundances and masses of atoms and molecules observed in emission. This table lists the g factor integrated over all transitions within the FOS spectral range for each species. Many of the spectra (Si I, Fe I, Fe II, and CS) are complex, consisting of many lines. For consistency, we used vacuum wavelengths throughout this paper.

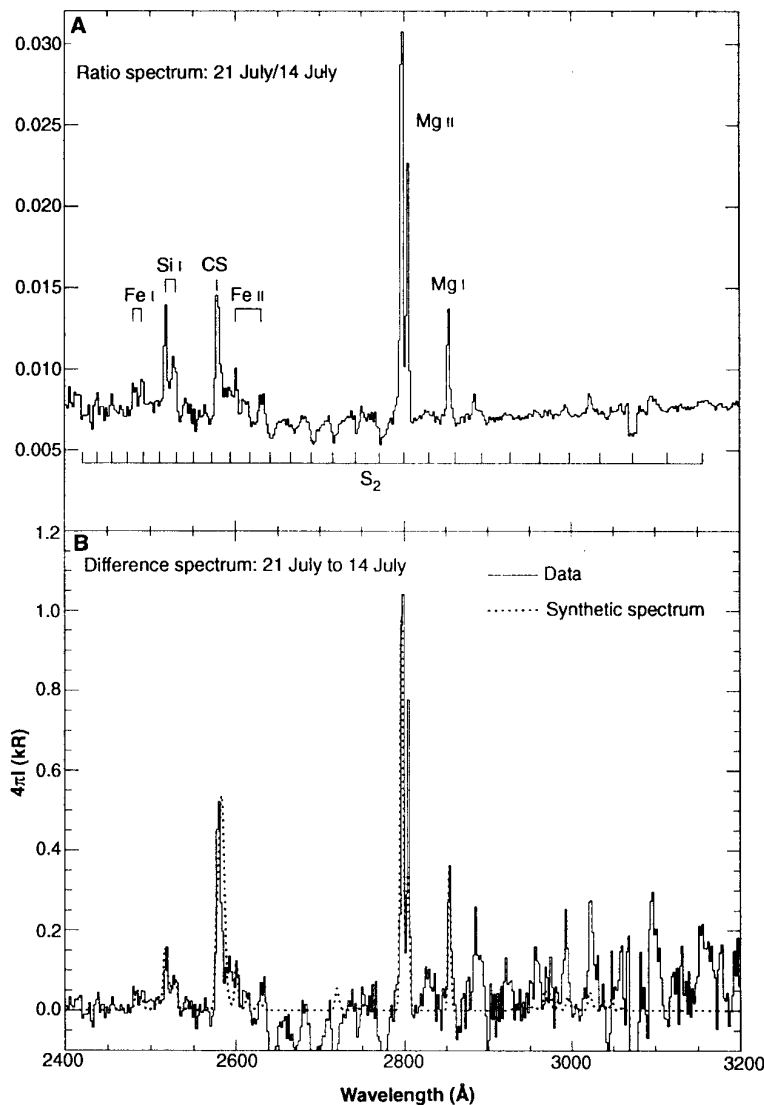| Atoms and molecules	g factor at 1 AU	Brightness (R)	Column abundance	Mass (g) in aperture	Mass (g) in 10^{15}-g comet
CS	5.8×10^{-4}	5000	2×10^{14}	8.6×10^{8}	3.6×10^{13}
Mg I	5.8×10^{-2}	1450	7×10^{11}	2.3×10^{6}	3.8×10^{13}
Mg II	1.9×10^{-1}	6300	9×10^{11}	2.9×10^{6}	3.8×10^{13}
Si I	8.1×10^{-3}	1100	4×10^{12}	1.5×10^{7}	8.1×10^{13}
Fe I	1.8×10^{-2}	700	1×10^{12}	7.6×10^{6}	4.5×10^{13}
Fe II	5.8×10^{-3}	1000	5×10^{12}	3.8×10^{7}	4.5×10^{13}

Figure 12.48– The near UV spectrum of the G impact SL9 impact site on 21 July. Easily visible are lines from Mg, Mg^{+}, Si, and Fe that most likely arise from the impactor itself. Table 12.10 (top) presents the masses of atoms inferred from these spectra as compared to the quantity of material available in the comet, showing that only a small fraction of the available metals are needed.
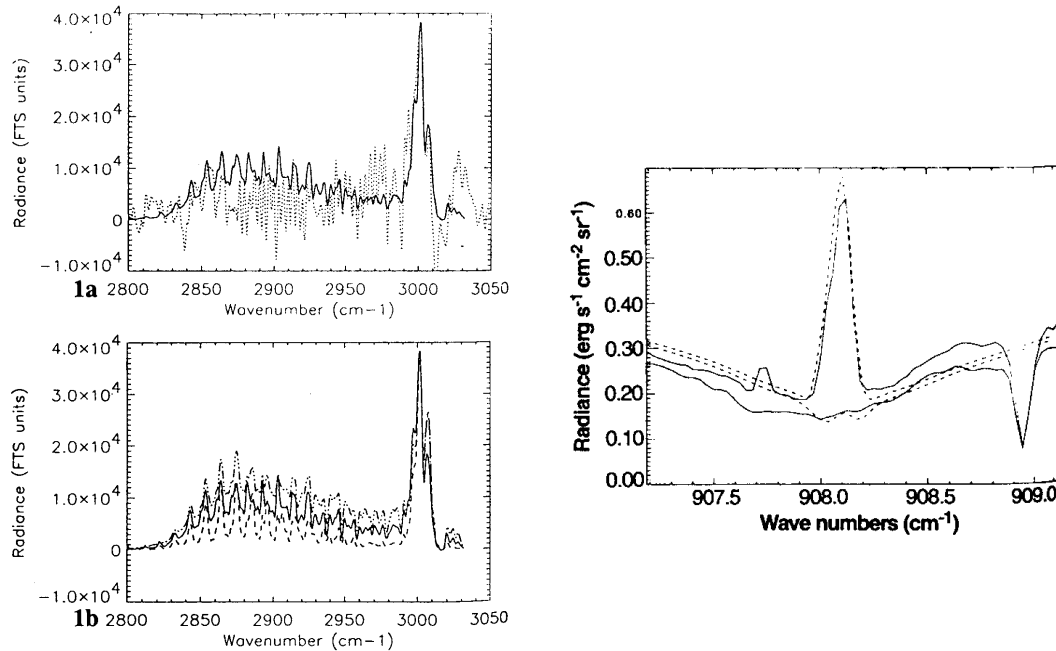
Figure 12.49– (Left) Spectrum of impact C on July 17:07:20 UT, at a resolution of 1700. The S/N is ∼10. The solid line is a best fit model using only CH_4, at P $= 10^{-4}$ bar, T $=$ 1000 K, D $= 50$ km; the impactor itself disintegrates somewhere near 50-100 mbar. (Right) NH_3 spectra at the K impact site (upper curves) and 6″ away (lower curves). Model fits are presented as dotted curves; the feature at 908.95 cm^{-1} is due to absorption in the Earth's atmosphere.
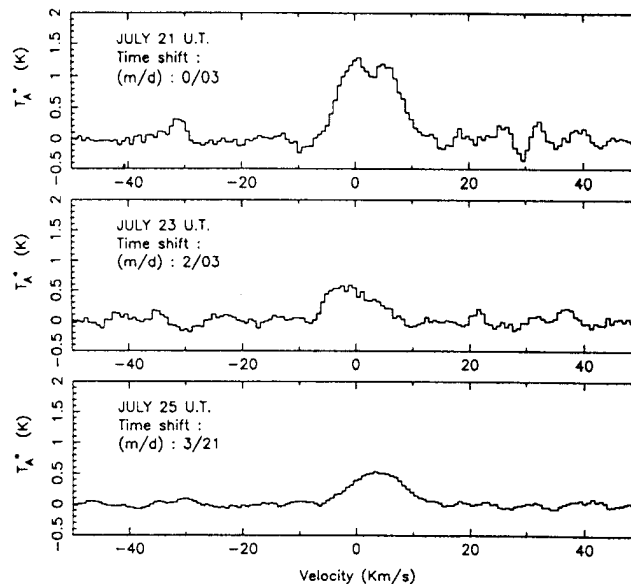

Figure 12.50– Millimeter-wave spectra of the HCN 3-2 line centered at 265.89 GHz, recorded on July 21, 23, and 25. In each case, the IRAM 30m telescope was tracking the impact site R.

b) The Terrestrial Planets

Spectroscopic studies of the terrestrial planets also cover the entire vacuum ultraviolet to millimeter/microwave range. Interestingly, at moderate resolution (and the moderate to low signal-to-noise ratios that would characterize the spectra of extra-solar planets), spectra of the terrestrial planets at infrared wavelengths can look surprisingly similar even though their atmospheric composition is quite different. To a large extent this arises because the dominant constituents of the earth's atmosphere, N_2, O_2, and Ar, are to a large extent spectroscopically inert unless one moves into the VUV. Thus, the *spectroscopically IR active* molecules are much the same.

To illustrate this point, the figures below present overview reflectance or emission spectra of Venus and the Earth in the near-IR. In this case, units are plotted as radiance or intensity, not temperature. The larger range results from the σT^4 dependence on temperature for greybody emission. At the higher signal-to-noise ratios which characterize the Galileo spectra presented below illustrate, differences do begin to emerge in the detection of features such as N_2O, CH_4, O_3 - which cannot exist in equilibrium and are evidence of the influence of life on the atmospheric composition. This is better illustrated by the nadir-viewing reflectance spectra from the LOWTRAN-7 satellite at optical/UV wavelengths. Note the tremendous change in scale (WHY?). Here oxygen and ozone are more visible, and are not seen in the spectra of the other terrestrial planets. Recall, however, that for most of earth history oxygen concentrations were rather low - as the figures to follow depict - so it is not clear that a young Venus and a young Earth can be easily distinguished from afar via spectroscopy. The history of terrestrial planets also depends on their size in that, so far as we know, the accumulation of substantial oxygen reservoirs in the atmosphere requires both life and an active tectonic cycle (to bury the organic carbon). On a small enough planet, the tectonic cycle can shut down after 1-2 AE (read Mars), and so on such bodies a detectable signal from oxygen or ozone may be a transitory phenomena.
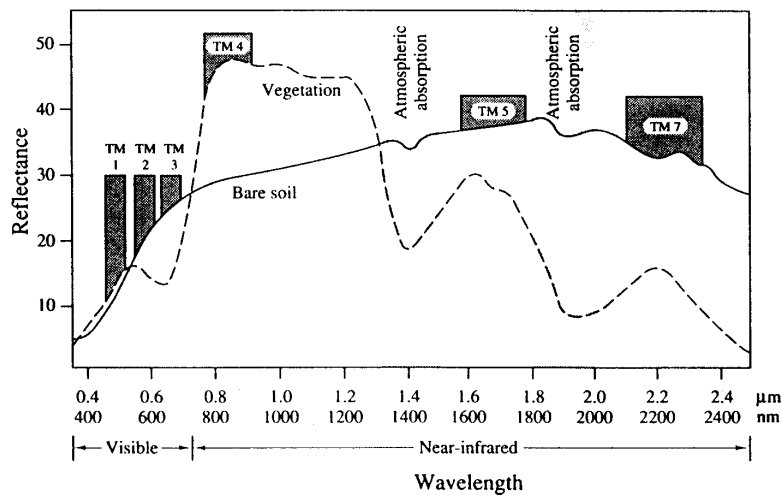

Figure 12.51– A portion of the solar reflectance spectrum of the Earth, showing the typical reflectance from soil (solid line) and leaf (dotted line) surfaces along with the regions of the spectrum that are measured by the LANDSAT satellite.
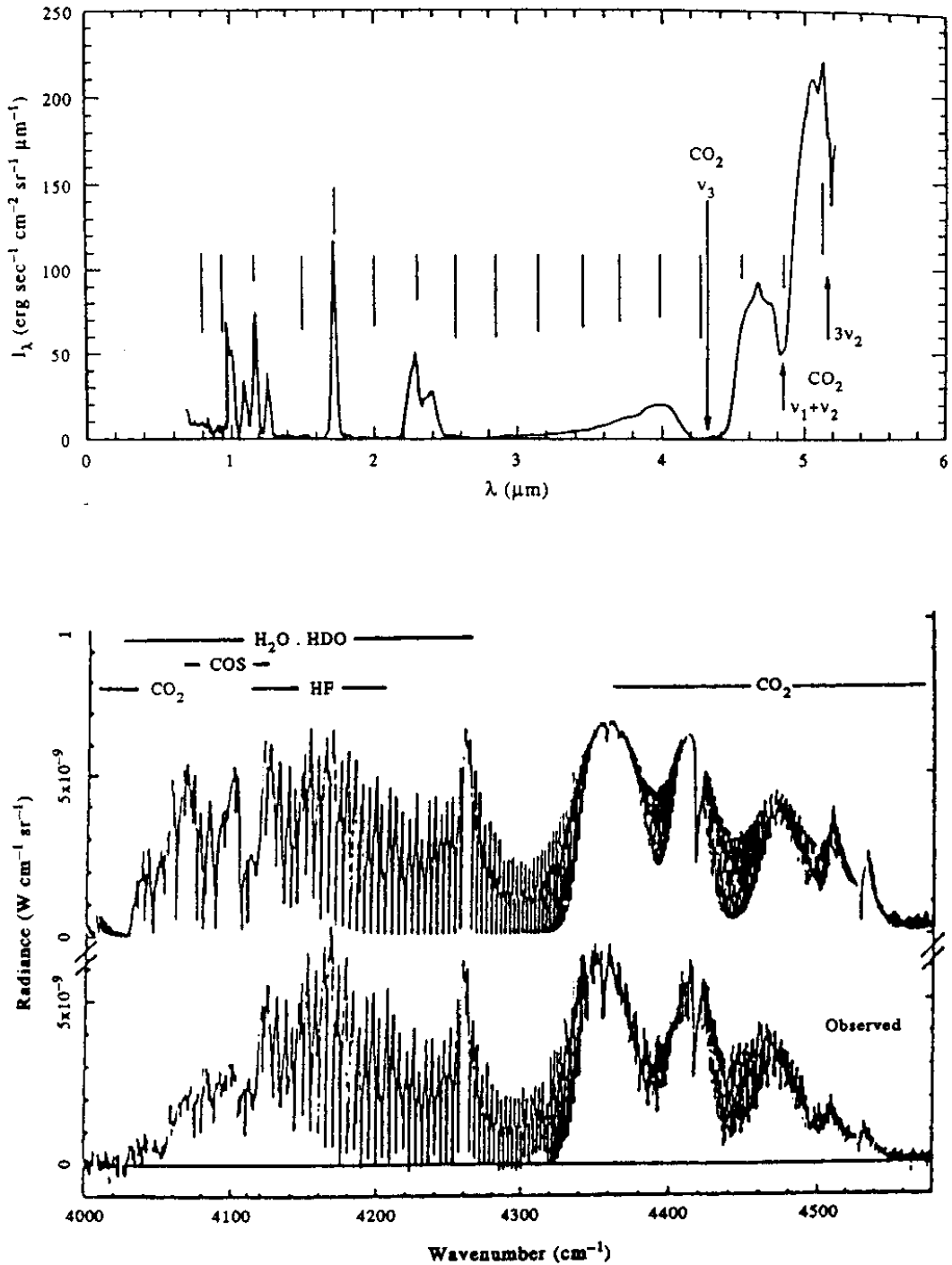
Figure 12.52– Typical spectra of the night side of Venus. The top spectrum presents a low resolution spectrum recorded across the near- to mid-IR by the NIMS experiment on board the GALILEO spacecraft. The bottom spectra were obtained at substantially higher resolution with the CFHT atop Mauna Kea, showing windows that reach into the lower part of the atmosphere (upper curve = model, lower curve = data).
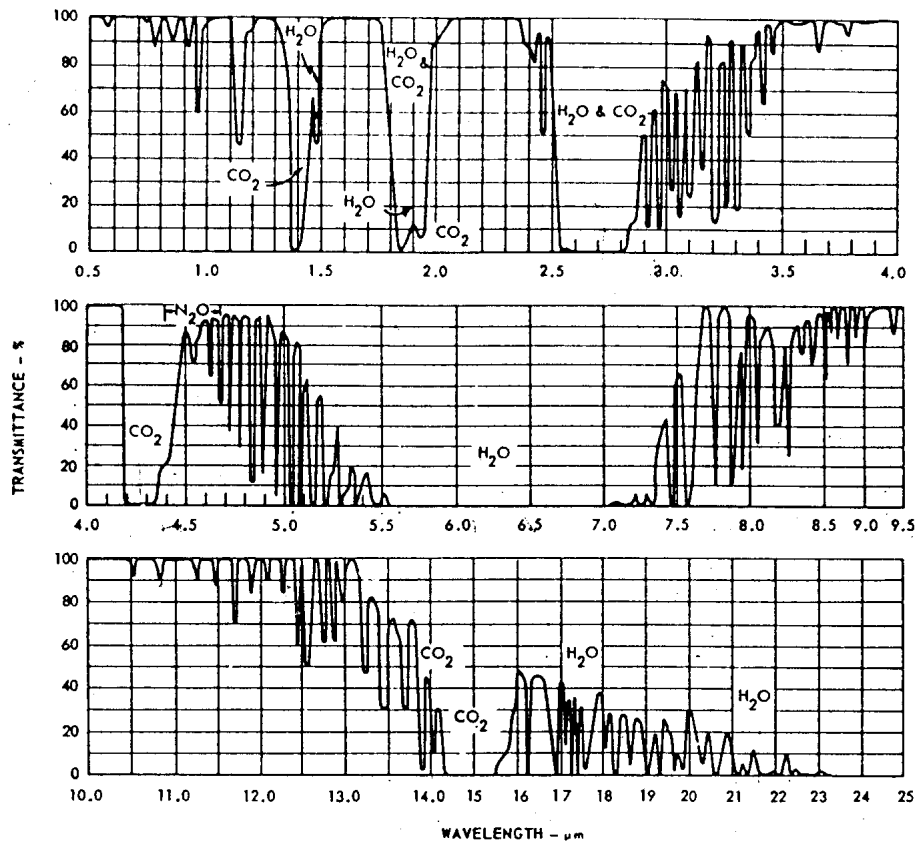
Figure 12.53– The transmission of a 1000 foot path in air at sea level containing 5.7 millimeters of precipitable water vapor. The temperature is 79 °F.
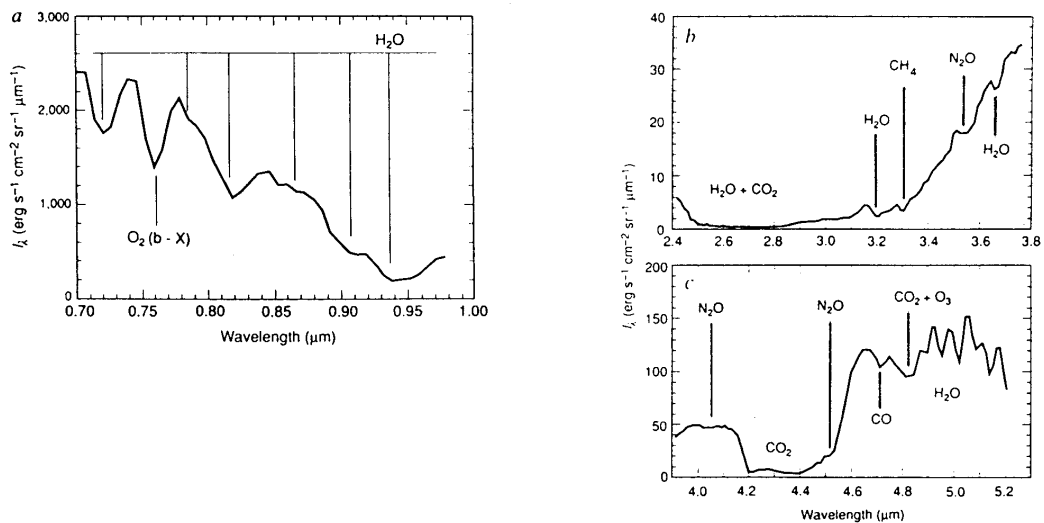

Figure 12.54– GALILEO spectra of the Earth over a relatively cloud free region of the Pacific Ocean, north of Borneo. A variety of both major and minor constituents of the atmosphere are visible, and the simultaneous presence of both reduced and oxidized gases can be used to infer the presence of highly non-equilibrium processes.
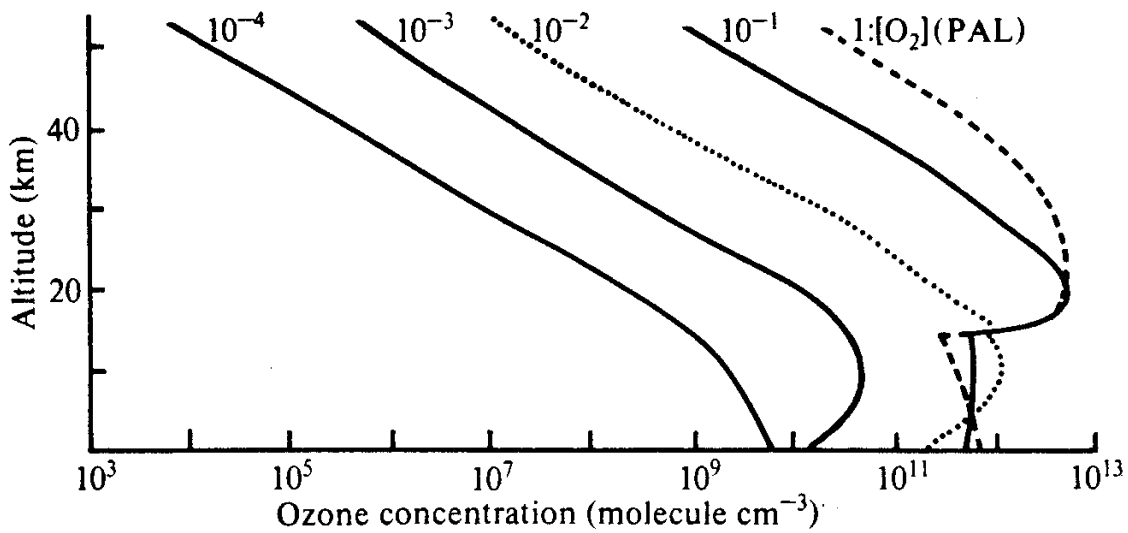
Figure 12.55– Vertical distribution of ozone for different total atmospheric oxygen contents ranging from the present atmospheric level (PAL) to 10^{-4} PAL. The model includes N, H, C, O, and Cl chemistry, and includes ozone loss at the planetary surface.
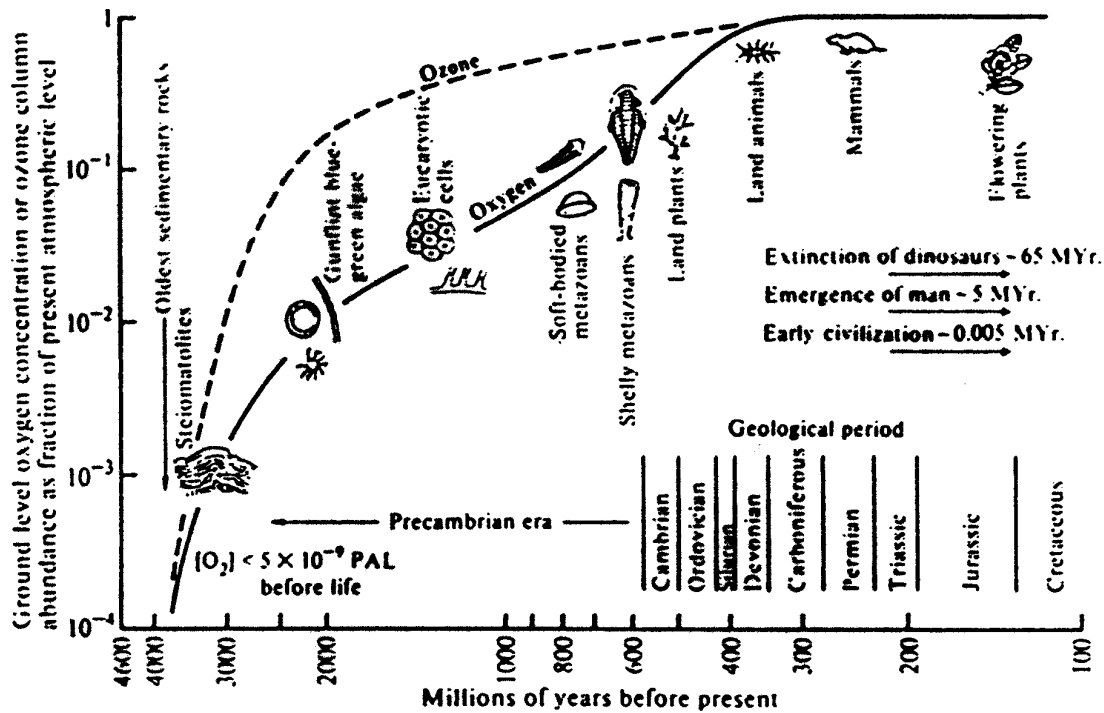

Figure 12.56– Evolution of oxygen, ozone, and life on Earth. In the absence of life, surface oxygen concentrations are unlikely to exceed $\sim 5 \times 10^{-9}$ of the PAL. Of the more than 3×10^{22} g of O_2 released by photosynthesis, 96% is contained in sedimentary rocks, beginning with the formation of the Banded Iron Formations (BIFs) about 3.7 AE ago. Eukaryotic cells need at least several percent PAL for respiration.